Experiments in Fluids (2006)
DOI 10.1007/s00348-006-0134-9

RESEARCH ARTICLE

Tobias Böhm · Philippe Frey · Christophe Ducottet
Christophe Ancey · Magali Jodeau · Jean-Luc Reboud

Two-dimensional motion of a set of particles in a free surface flow with image processing

Received: 22 April 2005 / Revised: 16 February 2006 / Accepted: 18 February 2006

Abstract A method to analyze bed load with image processing was developed. The motion of coarse spherical particles on a mobile bed entrained by a shallow turbulent flow down a steep channel was filmed with a high-speed camera. The water free surface and the particle positions were detected combining classical image processing algorithms. We developed a particle-tracking algorithm to calculate all particle trajectories and motion regimes, rolling or saltation. At constant slope, the contribution of the rolling particles to the solid discharge only slightly differed when the particle supply was increased. At a slope of 10%, it represented about 40%. In contrast, rolling became the major regime when the slope increased, at a slope of 15% it represented up to 80% of the total solid discharge.

Electronic Supplementary Material Supplementary material is available for this article at http://dx.doi.org/10.1007/s00348-006-0134-9 and is accessible for authorized users.

T. Böhm (✉) · P. Frey · M. Jodeau
ETNA, Cemagref Grenoble, BP 76,
38402 Saint-Martin-d'Hères Cedex, France
E-mail: tobias.boehm.1976@web.de
Fax: +33-47-6513803

C. Ducottet
Laboratory TSI, UMR CNRS 5516,
University of Saint Etienne, 10 rue Barrouin,
42000 Saint Etienne, France

C. Ancey
Swiss Federal Institute of Technology,
Ecublens, 1015 Lausanne, Switzerland

J.-L. Reboud
Université Joseph Fourier, LEMD,
25 av des Martyrs, 38042 Grenoble, France

1 Introduction

This paper presents a method to capture the motion of particles and the evolution of both the free surface and the bed of a two-phase flow using image processing.

Bed load transport in water courses remains difficult to study. Many researchers and practitioners have tried to calculate the transport rate as a function of the water flow. Empirical formulas such as the Meyer-Peter Müller formula (Meyer-Peter and Müller 1948) were established. These laws correctly predict the transport rate under steady uniform conditions well above the incipient motion threshold, but they yield poor results for more general flow conditions.

This motivates the search for a better understanding of the physical mechanisms governing bed load transport. The idea of considering bed load transport not as the flux of a continuous phase but as the superimposition of the motion of individual particles has thus gained new attention in the last few decades (Wiberg and Smith 1985; Schmeeckle and Nelson 2003).

Our contribution to this issue is an experimental study of the phenomena of bed load transport. Using a two-dimensional model channel we are able to investigate in detail the three motion regimes: saltating, rolling, or resting particles. If a coarse particle is set into motion it typically starts to roll and slide along the bed, when accelerated, it performs a series of leaps called saltation. Initially, we investigated these motion regimes of a single particle in a water flow (Ancey et al. 2002; Ancey et al. 2003). In the present study, we supplied the channel continuously with sediment (spherical glass beads). We were able to take sophisticated measurements by means of image processing and analyze the results from a physical point of view. We paid special attention to the rolling and saltating regime of particles. In particular, we will see that the rolling regime plays an important role in bed load transport, which has often been neglected (Bagnold 1973).

Image processing has been used for a variety of problems such as surveillance, scene monitoring (Courtney 1997), distortion measurement, and particle image velocimetry (Nishino et al. 1989; Willert and Gharib 1991). In the field of bed load transport, several authors have used photography and video techniques to investigate the motion of saltating particles but mostly at low slopes, low concentration and rarely under bed-load equilibrium on a mobile bed (Hu and Hui 1996a, b; Lee et al. 2000; Niño et al. 1994). Incipient motion of bed load has also been specifically addressed (Pilotti et al. 1997; Papanicolaou et al. 1999). The work of Drake et al. (1988) based on photography of bed load motion in a creek is particularly noticeable as the motion of particles occurred mainly by rolling.

For the present study we used the image-processing software Wima developed by the Traitement du Signal et Instrumentation laboratory (University of Saint Etienne, France). At Cemagref, the Wima software was used to derive turbulent velocity profiles with PIV (Frey and Reboud 2001), to measure the grain size distribution instantaneously at the outlet of a gravel-bedded channel (Frey et al. 2003), and to detect the motion of a single particle (Ancey et al. 2002, 2003).

The position of the water line can be extracted with classical image-processing operators: image thresholding and morphological operations (Gonzalez and Woods 1992). On the other hand, determining particle trajectories requires specific development: first we had to detect particle positions and second track the particles along the sequence in order to find the trajectories. The problem of object detection and localization in a gray scale image is known as a pattern-matching problem. It is usually solved using correlation techniques. More sophisticated nonlinear operators can also be used (Barat et al. 2003). The problem of tracking particles along a sequence is not trivial. Depending on the hypotheses made on particle displacement, more or less complex approaches have been proposed (Sethi and Jain 1987; Salari and Sethi 1990; Economikos et al. 1990; Hwang 1989).

The paper is structured as follows: after a presentation of the experimental facilities, we describe the detection algorithms used to calculate the water free surface and the particle positions. The particle-tracking algorithm developed to calculate the particle trajectories is presented. Three motion regimes of the particles (rest, rolling, or saltating motion) are defined and the bed elevation is calculated. After discussing the variables characterizing the transport, we analyze the water and bed surface elevations. Then, we study the vertical profiles of the solid discharge at a constant slope. Finally, we analyze the contribution of the rolling and saltating particles to the solid discharge for different slopes.

2 Experimental facilities

Bed load experiments were conducted in a narrow, glass-sided channel, 2 m in length and 20 cm in height (see Fig. 1). The slope could be adjusted within a range of 7.5–15%. The channel was continuously supplied with water and spherical glass beads with a diameter $d = 6$ mm and a density ρ_p of 2,500 kg/m^3. As the channel ($W = 6.5$ mm) was only slightly wider than this diameter, the particle motion was approximately two-dimensional. An obstacle at the channel outlet prompted the particles to settle on the rough channel base to form a bed of three particle layers on average over most of the channel length. The water flow rate per unit width q_w and the particle injection rate $\dot{n}_0$ were adjusted at the upstream entrance to obtain bed load equilibrium (see, Böhm 2005, for details on the experimental procedure).

Once equilibrium was reached, the particles and the water stream were filmed using a Pulnix partial scan video camera (progressive scan TM-6705AN). The camera was placed perpendicular to the glass panes 115 cm from the channel, approximately 80 cm upstream from the channel outlet. It was inclined at the same angle as the channel. Lights were positioned in the backside of the channel. An area approximately 25 cm in length and 8 cm in height was filmed and later reduced to accelerate image processing.

The camera resolution was 640 × 192 pixels for a frame rate of $f = 130$ fps (exposure time: 0.2 ms, 256 gray levels). Sequences of 8,000 images corresponding to a duration of approximately 1 min were acquired. Figure 2 shows typical images; a video sequence is available for download.

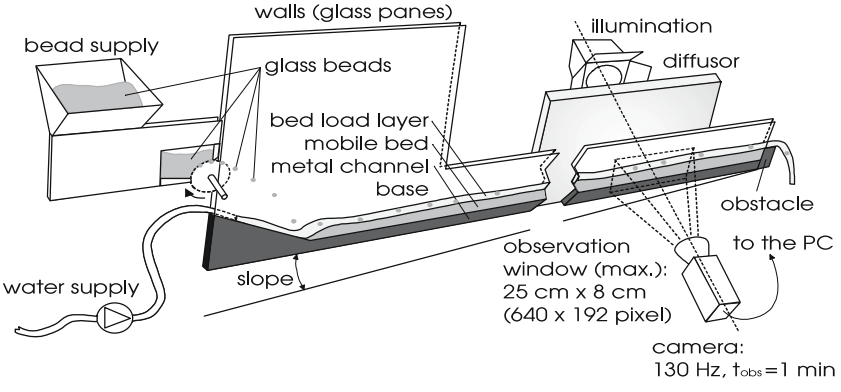

Fig. 1 Sketch of the experimental setup (after Böhm et al. 2004)

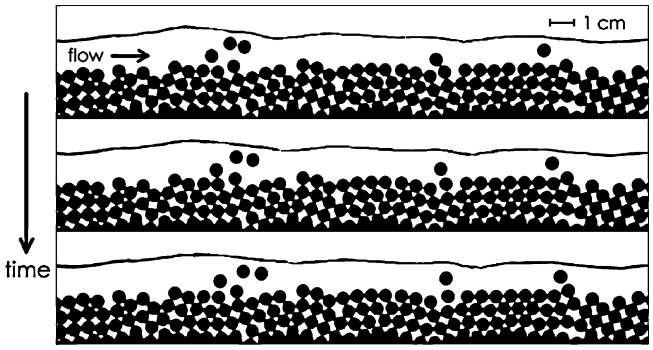

Fig. 2 Images of the particle transport. Image dimensions: 25 cm × 5 cm; frame rate: $f = 129.2$ Hz, channel slope: $\tan\theta = 10\%$, mean solid discharge $\dot{n} = 7.93$ beads/s, water discharge per unit width $q_w = 5.39 \times 10^{-3}$ m^2/s (after Böhm et al. 2004)

3 Image processing

A flowchart of all processing steps is given on Fig. 3.

3.1 Detection of the water free surface

The water free surface was fairly constant over the small width of the channel. In spite of the capillary attraction between water and the glass walls, the meniscus appeared on the filmed images as a thin line. We were thus able to take the mean value in the direction perpendicular to the channel walls to calculate the instantaneous water line as a function of the x-coordinate and time, $w_f(x, t)$.

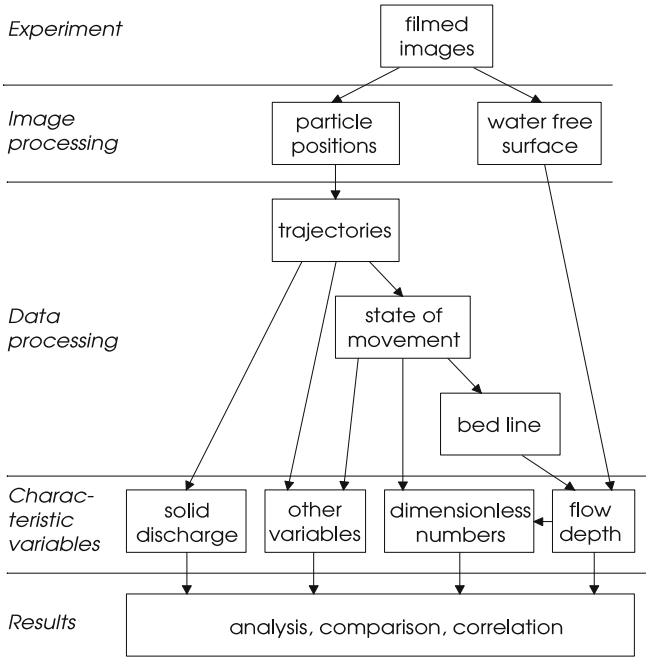

Fig. 3 Flowchart of image and data processing

We explain the procedure by considering a single image of the sequence reduced in length. Classical image-processing operators were used (Gonzalez and Woods 1992; Soille 1999). The processing was done in several steps, most of them appearing in Fig. 4:

(a) The image of the empty channel was subtracted from the image of the flow, the channel base was thus eliminated.
(b) The image was inverted and thresholded. The threshold value was chosen as a function of the luminosity and contrast of the source images.
(c) The white zones were eroded (four iterations) so the water line would disappear.
(d) Conversely, the resting white spots were dilated (six iterations) to join the zones before inverting.
(e) The logical AND-operation was applied on images (b) and (d). The particles were thus eliminated; the water line and small spots of noise remained.
(f) The line was slimmed down to the width of one pixel. It was then scanned from the top to find the first white pixel of each column to obtain $w_f(x)$. Figure 4e shows that there were some missing portions due to light reflections of the free surface. Consequently, we rejected the values breaching the condition $|w_f(x) - \overline{w_f(x)}|$ where $\overline{w_f(x)}$ is the x-averaged value and a maximal elongation of $w_e = 15$ pixels was chosen. The rejected values were recalculated making use of their neighboring zones. Inside the image, we applied linear interpolation. If there were missing portions at the left or right edge of the image, $w_f(x)$ was set to the value of the nearest available point (extrapolation with a constant value).

The uncertainty of the water line position was in most instances less than 1 pixel.

3.2 Detection of the particle positions

To detect the particle positions, we used the image of a model bead (Fig. 5b) in addition to the filmed image (Fig. 5a). A correlation between the model and the image was computed (Gonzalez and Woods 1992). A ring-shaped model was chosen with negative values inside in order to have a zero mean value. A bead was detected whenever it coincided with the ring. The diameter of the ring was chosen to match the diameter of the beads in the filmed image. The algorithm thus made use of the uniform size and shape of the particles. The processing steps are illustrated in Fig. 6:

(a) An algorithm to search the pattern (Fig. 5b) in the image was applied. We obtained an image showing the zones of high and low correlations in light and dark grays, respectively. Note that the correlation coefficient could not be calculated close to the image edges. Here the resulting image pixels were set to a medium gray level. The width of this zone was half

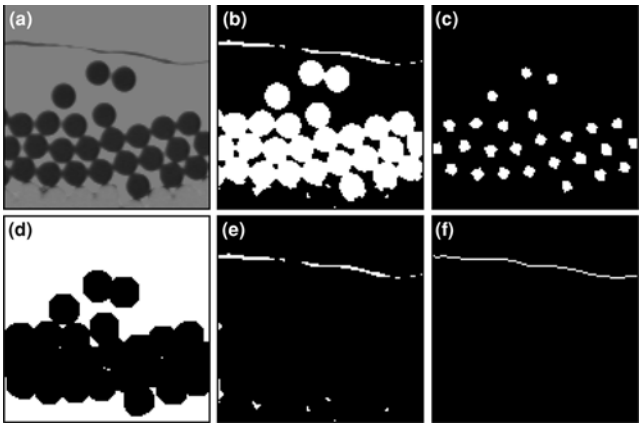

Fig. 4 Detection of the water line. Image-processing steps

the size of the model bead image (16 pixels). In the center of Fig. 6a, a "correlation cloud" can be seen for each bead in the original image. Although these clouds intersected, circular shapes with pronounced maxima were obvious.

(b) The local maxima of the image were retained, i.e., all the pixels that were lighter than their four neighbors. In the figure, they are shown as white crosses. Since the model bead fitted very well the filmed beads and image noise was very low we did not have any problems with spurious detection of particles.

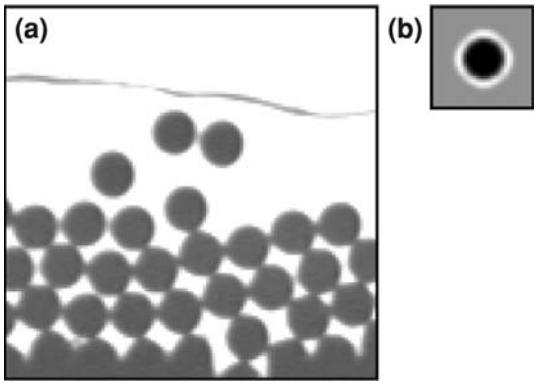

Fig. 5 Detection of the particle positions. Original images

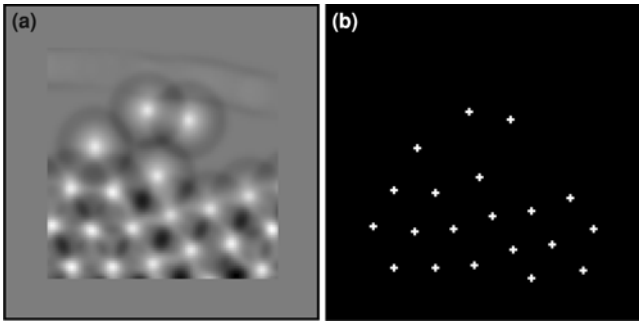

Fig. 6 Detection of the particle positions. Image-processing steps

(c) The (x,y)-positions of these crosses were extracted and saved in a list associated with the image (not shown in the figure).

The uncertainty of the detected particle positions was on the order of 1 pixel (0.387 mm).

4 Particle tracking

4.1 Overview

A particle-tracking algorithm was developed to obtain the particle trajectories from the particle position data. The particle image velocimetry is perhaps the most popular recent technique in experimental fluid mechanics. A related method used especially for low particle concentrations is particle-tracking velocimetry (Nishino et al. 1989; Udrea et al. 2000). Its usual application is the determination of the velocity field of a fluid carrying small particles. In contrast, we focused on the individual particle motion in our study. The particle velocities differed from those of the surrounding fluid since our particles were coarse and had a higher density than water. Our algorithm was nevertheless comparable to algorithms developed by Sethi and Jain (1987), Economikos et al. (1990) and Okamoto et al. (1995): it uses the principle of prediction to select candidates for an association and a cost function to choose the best one.

The algorithm compared the bead positions of two consecutive images to determine the trajectory of each bead step by step. Although the use of spherical particles of uniform size made detection easier, it hampered the calculation of the trajectories since we were unable to distinguish between particles because of their shape. Given the high frame rate of the camera, the displacement of a particle between two images was always smaller than a particle diameter. This was essential not only to reach a high resolution of the trajectories, but primarily to be able to distinguish the particles over time. We explain the algorithm by describing first its initial step and then the iteration step, which was simply an advancement of the initial step.

4.2 Initial step

The initial time step of the particle-tracking algorithm is illustrated in Fig. 7. For each particle of the first image, we defined a circular searching zone (here shown only for particles A and B). The radius of this zone was the maximal displacement expected. A particle of the second image was associated with a particle of the first image if it was lying inside its search perimeter. Here, particle D was associated with B, whereas C was associated both with A and B. For each association, we noted the distance of the particles (see Table 1).

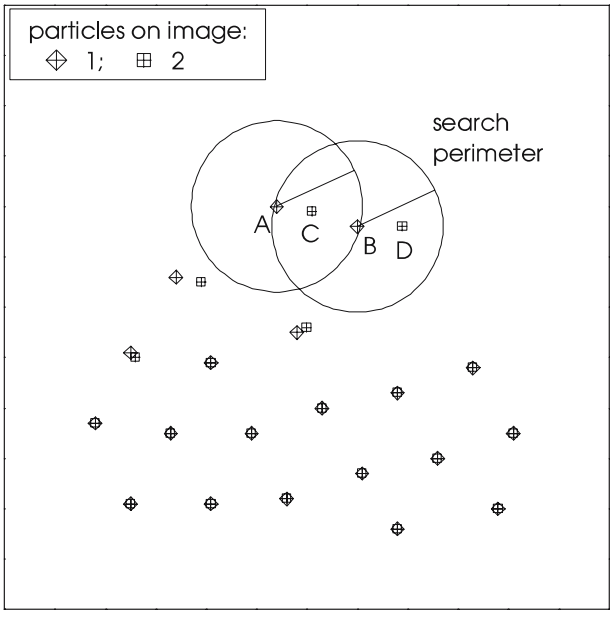

Fig. 7 Initial time step of the particle-tracking algorithm

After the calculation of the complete association table for the image couple, the best associations were selected. For this purpose, the association with the minimal distance was chosen, eliminating other possible associations of the involved particles. In the case of several minimal distances, one of these associations was chosen arbitrarily. Next, the best remaining association was selected. In our example, the association A–C was chosen first; as a consequence, this eliminated the association B–C. In a second iteration, the association B–D was selected. Note that for some particles, no predecessor or successor could be found, especially for the particles entering or leaving the observation window.

In this way, the association table was transformed into a table of trajectories of the particles for the first two images. The information on particle displacements was used for the following calculation step.

4.3 Iteration steps

A sketch of the particle-tracking algorithm for the following time-step is displayed in Fig. 8. It shows the particle positions for images 2 and 3. The difference compared to Fig. 7 is the position of the searching zones. An estimate for the particle position in image 3 was obtained by adding the displacement vector of the preceding calculation step to each particle position in image 2 (black arrows). The searching zone was centered around this estimate. Thus, the algorithm made use of the low acceleration of the particles.

Apart from the positions of the searching zones, the algorithm worked as described above. Here, the distance was calculated between the particle position of the third image and the estimated position (see Table 2). As the

Table 1 Association table for the initial time step

Particle on image 1	Particle on image 2	Distance (pixels)
A	C	7.07
B	C	9.49
B	D	9.00
...		

calculated distances were considerably lower for the second calculation step, a better correlation was achieved. In our example, particles E and F were associated only with particles C and D, respectively. The positions of particles E and F were appended to the trajectories, which then were denoted by A–C–E and B–D–F, respectively.

Whenever the information of the last displacement was available, it was used to calculate the estimate of the new particle position. If no predecessor of a particle could be found, a new trajectory was created. Otherwise, the particle coordinates were appended to an existing trajectory. If no successor position of a particle was found the trajectory was closed.

The only arbitrary parameter of the algorithm was the radius r of the searching zone, which was nothing but the maximal expected particle displacement. To avoid the association of resting particles with their neighbors, we limited it to the particle diameter on the images, $r = d/s \approx 16$ pixels, where s denotes the scaling factor of the camera. This limited the particle velocity being detected by the algorithm: $v_m = r\,s\,f \approx 0.80$ m/s, where v_m denotes the maximal velocity and f the frame rate of the camera. The limit affected only the first calculation steps of the trajectories whose particles were entering the observation window. The following steps

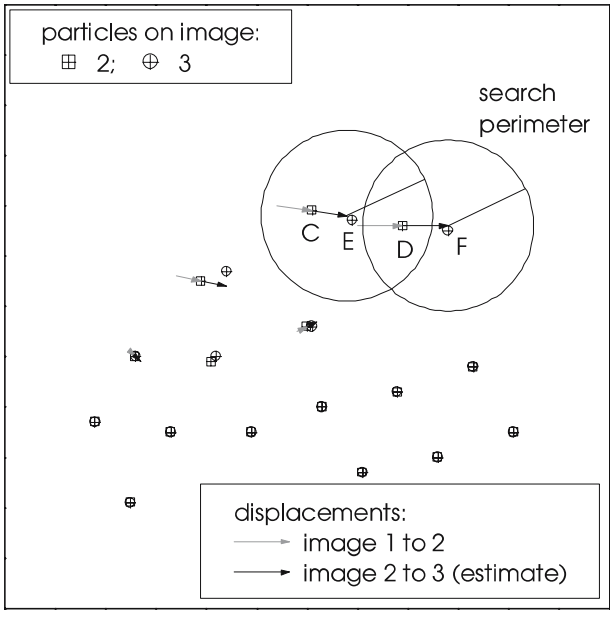

Fig. 8 Iteration time step of the particle-tracking algorithm

Table 2 Association table for an iteration time step

Particle on image 2	Particle on image 3	Distance (pixels)
C	E	1.41
D	F	1.00
...		

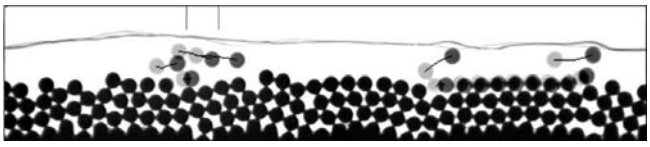

Fig. 9 Visualization of the particle trajectories (*black*). In the background, the particles at the initial (*light gray*) and the final positions (*dark gray*) of the short image sequence are shown

were simple since the preceding displacements could be taken into account for tracking. Since the particle velocities in our experiments rarely exceeded 0.5 m/s, almost all the trajectories could be tracked from the start at the left edge of the image. Indeed, we calculated the trajectories on the whole images (640 pixels in the x-direction) but restricted the final analysis to a smaller zone. Zones of 30 pixels were cut off from the left and the right, leaving an effective image length of 580 pixels.

4.4 Trajectories

Running the algorithm on the whole image sequence, we obtained a table with the trajectories of all the particles observed. This table contained 400–2,000 trajectories, depending on the solid discharge adjusted at the channel entrance. Table 3 shows a considerably shortened example of a trajectory table. The lists of x- and y-positions do not represent regular arrays since the trajectories had different sizes (the size of a trajectory being the number of time steps it was tracked). We thus had to note the time step of the start and the size of each trajectory in the table.

In the example, the particles involved in trajectories number 4–8 did not move at all during the five time steps. Particles 1 and 3 entered the observation zone, whereas particle 2 left it.

Figure 9 shows the trajectories of the first five time steps of an image sequence. The first and the fifth filmed images can be seen in the background (the particles are shown in light and dark gray, respectively). The zone in the x-direction of Table 3 is marked in the upper part of the figure for a comparison.

While developing the particle-tracking algorithm, we tested its accuracy continuously. We used reduced image sequences to compare the calculated trajectories with the filmed images. The algorithm yielded correct results even when particles collided. The amount of data extracted from our experiments was still too large to make more than random sample tests of the reliability of the trajectories. Additionally, we carefully studied the global results obtained from the analysis of the trajectories. We especially compared the solid discharge deduced from the trajectories $\dot{n}$ with the injection rate $\dot{n}_0$. This measured solid discharge fluctuated greatly. However, taking the average over sufficiently long time periods (1 min), the relative difference $(\bar{\dot{n}} - \dot{n}_0)/\dot{n}_0$ was smaller than $\pm$ 3% (see Table 4). We can thus conclude that the algorithm performed accurately for the given problem.

5 State of movement and bed line

5.1 Definition of the state of movement

Next the state of movement of a particle was defined by considering that each bead was always either in a resting, rolling, or saltating regime (see Fig. 10). This partitioning posed several difficulties from the algorithmic viewpoint. The three states of movement were distinguished as follows:

The resting beads formed the bed, they were in sustained contact with their neighbors. They were not expected to move or, more precisely, their possible drift velocities (together with fluctuating velocities) were lower than a threshold velocity u_t: $|\mathbf{u_p}| < u_t$, where $\mathbf{u_p}$

Table 3 Example for a table of trajectories. Number, start, and size are the number of the trajectory, the first time step of its tracking, and the number of time steps the particle was tracked, respectively

Number	Start	Size	x-Positions (pixel)				y-Positions (pixel)					
1	2	4	–	194	202	209	217	–	41	43	45	47
2	1	3	203	212	221	–	–	44	44	45	–	–
3	2	4	–	193	194	196	199	–	64	64	64	64
4	1	5	211	211	211	211	211	77	77	77	77	77
5	1	5	196	196	196	196	196	80	80	80	80	80
6	1	5	219	219	219	219	219	90	90	90	90	90
7	1	5	204	204	204	204	204	93	93	93	93	93
8	1	5	211	211	211	211	211	104	104	104	104	104

The table was made for a reduced zone in x ($193 < x \leq 223$ pixel) and only for the first five time steps

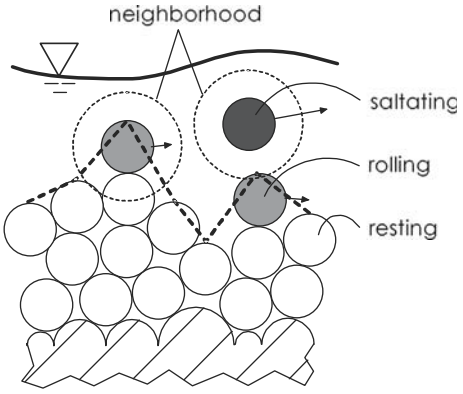

Fig. 10 Sketch defining the state of movement and the bed line

denotes the particle velocity averaged over five consecutive frames.

The beads in the rolling regime were located above the beads at rest: they remained in close contact with the bed and moved at a certain velocity. Our algorithm used two criteria to distinguish rolling beads: $|\mathbf{u_p}| \geq u_t$ (bead in motion) and $d_n/d \leq \varepsilon$ (particles in the vicinity), where d_n is the distance to the next neighbor (measured between the mass centers and averaged over five consecutive frames) and ε is a threshold.

The beads in saltation leaped above the others. They had no close neighbors except when they collided with other beads. The algorithm distinguished saltating beads using the criteria $|\mathbf{u_p}| \geq u_t$ and $d_n/d > \varepsilon$.

The values of the threshold parameters u_t and ε were adjusted by trial and error to minimize the differences between the state determined by the algorithm and the state determined by the naked eye. Good agreement was obtained for $u_t = 0.025$ m/s and $\varepsilon = 1.07$.

The state of movement of each particle was a function of time. A particle at rest could be set in rolling motion by the fluid or other particles and accelerated to get into saltating motion. On the other hand, a fast moving particle could lose its kinetic energy and come to rest.

5.2 Definition of the bed line and water depth

While the free surface line was relatively easy to define and detect with classical image algorithms, the bed line $b_s(x, t)$ was more difficult to define because it was continuously evolving through particle deposition and erosion. In addition the low submergence that is the ratio of water depth to the bead diameter made this definition crucial. As rolling particles had a very low velocity compared to the mean water velocity, we considered that the bed surface profile is the broken line linking the top points of the uppermost resting or rolling beads. Figure 10 depicts this broken line at a given time.

The water depth $h(x, t)$ was then defined as the difference between the water and the bed elevation, $h(x, t) = w_f(x, t) - b_s(x, t)$.

6 Results

Table 4 reports time-averaged values for experiments with slopes ranging from 7.5 to 15%. These experiments were run with different particle injection rates $\dot{n}_0$ by adjusting the water discharge each time in order to obtain bed load equilibrium.

We express the solid discharge in beads per second and define it as a function of time:

$$\dot{n} = \frac{1}{L}\sum_{i=1}^{N} u_i.$$

L, N, and u_i are the horizontal length of the observation window, the number of the observed particles, and the x-component of the individual particle velocity, respectively. The solid discharge thus represents the cumulated motion of the particles in the observation window. The time evolution of the solid discharge was studied in (Böhm et al. 2004); here we present only the mean values.

The flow Reynolds number is defined as $\mathrm{Re} = 4R_h\bar{u}_f/\nu$, where $R_h = Wh/(2h + W)$ denotes the

Table 4 Flow characteristics and time-averaged values of dimensionless numbers characterizing bed load and water flow

Experiment	E7-6	E7-8	E7-9	E10-6	E10-8	E10-21	E12-9	E12-16	E12-21	E15-16	E15-21
$\tan\theta$ (%)	7.5	7.5	7.5	10	10	10	12.5	12.5	12.5	15.0	15.0
$\dot{n}_0$ (beads/s)	5.7	7.8	8.7	5.3	8.0	20.0	9.3	15.2	20.0	15.6	21.5
q_w (10^{-3} m^2/s)	10.00	11.54	13.85	4.15	5.39	10.31	2.97	3.85	4.46	2.31	2.92
h (mm)	18.9	20.8	24.9	10.0	12.0	19.4	7.0	8.2	9.4	4.9	6.7
σ_h(mm)	2.2	2.3	2.5	2.1	2.3	2.7	2.2	2.3	2.4	2.0	2.5
u_f (m/s)	0.53	0.55	0.56	0.42	0.45	0.53	0.42	0.47	0.48	0.47	0.44
$\dot{n}$ (beads/s)	5.45	7.76	9.20	5.21	7.93	20.65	9.52	15.52	19.86	15.45	20.55
Re	5,860	6,230	6,400	4,090	4,590	5,920	3,760	4,360	4,600	3,680	3,830
Fr	1.23	1.22	1.13	1.30	1.27	1.21	1.60	1.66	1.58	2.14	1.72
N_{Sh}	0.158	0.173	0.207	0.113	0.135	0.216	0.098	0.114	0.130	0.082	0.111
C_s (%)	0.95	1.17	1.16	2.18	2.56	3.49	5.58	7.02	7.74	11.65	12.23
h/d	3.16	3.47	4.15	1.66	2.00	3.23	1.17	1.37	1.56	0.82	1.11
κ_r (%)	29.0	28.6	31.1	38.2	36.1	41.8	68.0	63.8	57.0	84.9	76.2
κ_s (%)	63.9	65.7	62.2	54.8	56.9	50.7	19.9	24.1	32.1	4.4	16.4

Varying parameters: channel inclination $\tan\theta$ and solid discharge $\dot{n}$. The mnemotechnic notation E7-6 indicates: $\tan\theta \approx 7\%$ and $\dot{n} \approx 6$ beads/s. Not all the experiments we performed are reported here

hydraulic radius, $\bar{u}_f = q_w/h$ the fluid velocity (averaged in the y- and z-directions), v the kinematic viscosity of water, and h the water depth. The values of the Froude number $Fr = u_f/\sqrt{gh}$ (where g denotes gravity acceleration) indicate a mean supercritical regime.

The solid concentration is defined as the ratio of the solid and the water discharge $C_s = \dot{n}v/(q_w W)$, where $v = \pi d^3/6$ is the particle volume. Compared with values found in sedimentology, the concentration was high due to the steep channel slope. The ratio h/d was low, in the range 1–4.

The Shields number is defined as the ratio of the bottom shear stress to the stress equivalent of the buoyant force of a particle lying on the bottom and reads $N_{Sh} = h \tan\theta/((\rho_p/\rho_f - 1)d)$.

Furthermore, we broke down the solid discharge into the contributions of the rolling (κ_r), and the saltating (κ_s) beads.

We present in this paper only three aspects of the results. We first investigate, for a single experiment, the features of the water free surface and the bed surface elevation. Secondly, we study the contribution of the rolling regime at a constant slope but for increasing flow rates by analyzing the vertical transport profiles. Finally, we show that rolling becomes the major regime when the slope increases. Further results can be found in Böhm et al. (2004, 2005).

6.1 Water and bed surfaces

In Fig. 11, the free surface elevation $w_f(x,t)$ (Sect. 1) for experiment E10-8 (see Table 4) has been coded in gray levels. The image represents the information of the full length of the observation zone, while only a short time period is shown here (2 s instead of 60 s). The representation of $w_f(x, t)$ in the form of an image facilitated, on the one hand, the visual interpretation and enabled, on the other hand, a further analysis with the image-processing software. An obvious feature of the diagram is the characteristic propagation velocity of the water surface waves of $c = \Delta x / \Delta t \approx 0.41$ m/s, which was close to the mean fluid velocity u_f given in Table 4.

We calculated the probability density functions (pdf) of w_f and the bed surface elevation b_s for the whole data sequence ($\Delta t = 61.9$ s, see Fig. 12). The pdf of w_f was narrow and nearly Gaussian (mean value $\bar{w}_f = 33.1$ mm, standard deviation $\sigma_{wf} = 1.9$ mm), which indicates that small positive and negative perturbations of the elevation occurred with an even frequency. In contrast, the pdf of b_s ($\bar{b}_s = 21.4$ mm, $\sigma_{bs} = 2.2$ mm) had a higher maximum and wider tails. While most of the time the bed line was at a level of 20–23 mm, occasionally it raised or fell considerably (on the order of one particle diameter). The former process can be attributed to particles that reposed momentarily on the quasi-immobile bed, the latter to sporadic rearrangements in the bed. Furthermore, calculation of intercorrelation functions between w_f and b_s showed that water and bed elevations were strongly coupled. The background of Fig. 12 was obtained by superimposing all the images of the filmed sequence.

6.2 Vertical transport profiles on a constant slope

In Fig. 13, the distributions of the solid discharge $\dot{n}$ in the vertical direction of the flow [solid curves (t)] are plotted for three experiments on a constant slope of 10%. Additionally, we show the individual contribution of the saltating (s), rolling (r), and resting (re) particles to the total solid discharge. The slope of 10% is indeed typical for torrents concerned by bed load phenomena.

The diagrams show three peaks at intervals of approximately one particle diameter. Experiment E10-21 (Fig. 13c) revealed a fourth peak one particle diameter above, the transport occupying here a wider y-range, as the water level was also higher. The occurrence of peaks in the transport profiles indicates that the particle bed had a layered structure. Although we paid special attention to designing an irregular channel base (see Fig. 2), the bed became ordered.

The peaks of Fig. 13 coincide fairly well with the presence of different transport regimes. In the lower part [small peaks (re)], particles moved at low drift velocities, i.e., in the resting regime. Each of the central peaks (r) (for Experiment E10-21 the two central peaks) for the most part represents the contribution of the rolling particles. The uppermost peaks (s) are essentially due to particles in saltation. A striking point is that the two lower peaks grew only little from (a) to (c), while the

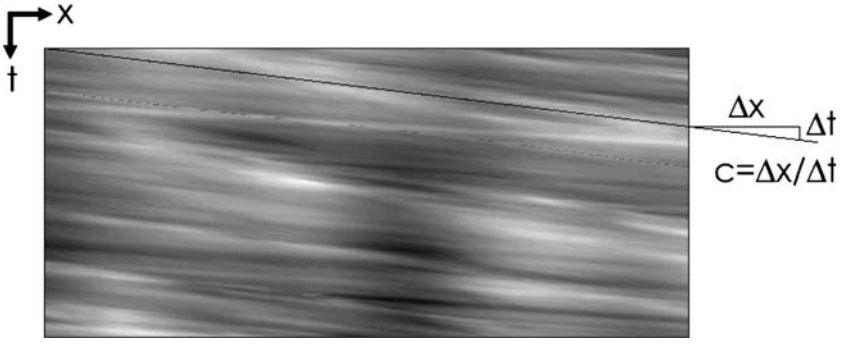

Fig. 11 Elevation of the water free surface $w_f(x, t)$ as a gray scale image. Image dimensions: $x_2 - x_1 = 220$ mm, $t_2 - t_1 = 2$ s. *White*: $w_f(x, t) = +5.7$ mm, *black*: $w_f(x, t) = -5.5$ mm versus the mean value. The *line* represents the characteristic propagation velocity of the surface waves c. For experimental conditions, see experiment E10-8 in Table 4

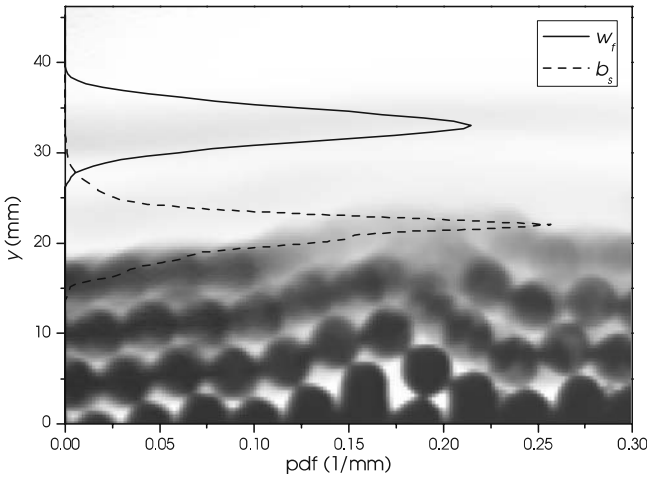

Fig. 12 Probability density functions (pdf) of the water free surface w_f and the bed surface elevation b_s. For experimental conditions, see experiment E10-8 in Table 4

uppermost peak grew considerably and produced another peak for experiment E10-21. A higher solid discharge was thus mainly achieved by an increase in the transport near the water free surface, while the particle transport below remained nearly constant.

The y-integrals of the dashed curves represent the weights of the different transport regimes. It is noticeable that the three experiments differed only slightly: the contribution of the saltating (κ_s) and rolling (κ_r) particles to the solid discharge did not vary much and were, respectively, 50–57 and 36–42% (see Table 4). The rolling regime was thus far from being a marginal mode.

6.3 Rolling and saltating regime for different slopes

When working at constant slope, there was almost no variation of the contribution of the saltating particles to the transport, κ_s. In contrast, this ratio turned out to depend on channel slope and water depth h or on the dimensionless number h/d (see Fig. 14). For $\tan\theta = 7.5\%$, κ_s was higher, but still constant (between 62.2 and 64.1%). We can thus conclude that for mild slopes (7.5 and 10%), κ_s was a function of $\tan\theta$ only. For steeper slopes though (12.5 and 15%), the diagram shows that κ_s was a linear function of h/d and decreased with $\tan\theta$, the rolling regime becoming dominant.

Surprisingly, the data show that saltation occurred even if the time-averaged water depth fell below one particle diameter. This was due to the fluctuations of h, since even in the extreme case $h/d = 0.82$ the instantaneous water depth frequently exceeded one particle diameter, which enabled saltation (see the whiskers in Fig. 14). To take the effect of water line fluctuations into account, we defined the efficient flow depth as $h + \sigma_h$ and we considered that the experimental trend for slopes in the range 10–15% could be described using the linear fit $(h + \sigma_h)/d$. This experimental trend at higher slopes suggests the existence of a threshold of saltation at $(h + \sigma_h)/d = 1$, as shown in Fig. 14 where the fitted straight line intersects the (h/d)-axis. Such an analysis was only possible because we measured the instantaneous water depth.

Dimensionless solid discharges ϕ_s as a function of Shields numbers N_{Sh} were plotted on Fig. 15. The solid discharge was made dimensionless by the definition:

$$\phi_s = \frac{q_s}{\sqrt{(\rho_p/\rho_f - 1)gd^3}},$$

where q_s is the bed load transport rate per unit width, $q_s = \pi d^3 \dot{n}/(6W)$. Two semi-empirical formulas were also plotted, the Meyer-Peter Müller formula (Meyer-Peter and Müller 1948) $\phi_s = 8(N_{Sh} - 0.047)^{3/2}$ and the Fernandez-Luque formula (Fernandez Luque and van Beek 1976) $\phi_s = 5.7(N_{Sh} - 0.06)^{3/2}$. Our data were quite scattered in this diagram, the points seemed to be affected by

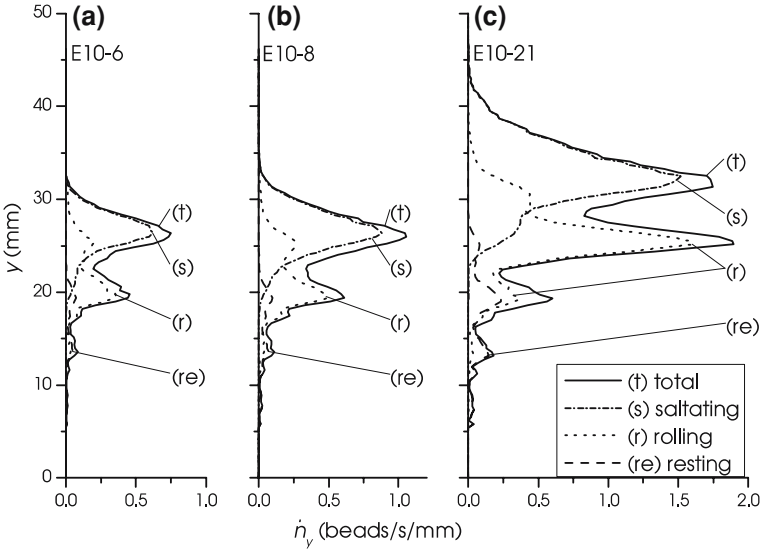

Fig. 13 Solid discharge $\dot{n}_y$ as a function of the y-coordinate (total solid discharge and elementary contributions) for experiments E10-6, E10-8 and E10-21. Varied parameters: solid discharge $\dot{n}$, water discharge per unit width q_w, water depth h. Constant parameter: channel slope $\tan\theta = 10\%$. For experimental conditions, see Table 4

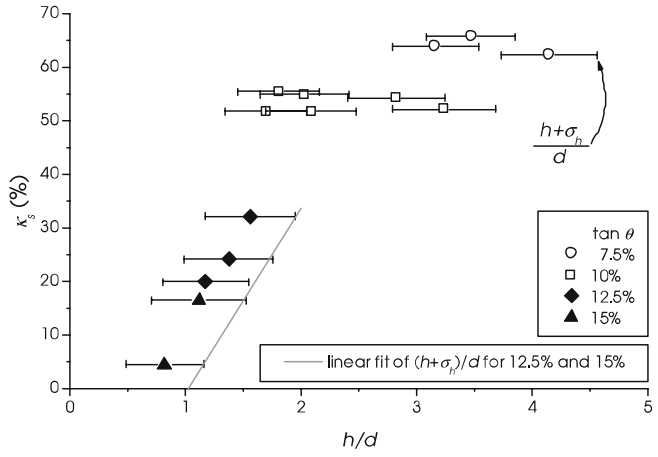

Fig. 14 Relative contribution of the saltating particles to the solid discharge κ_s as a function of the ratio h/d, where h and d are the water depth and the particle diameter, respectively. The whiskers represent the standard deviation $(h \pm \sigma_h)/d$

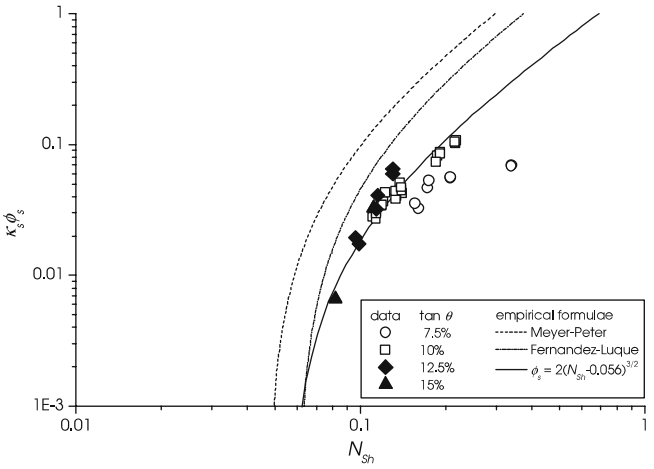

Fig. 16 Dimensionless solid discharge due to the saltating particles, $\kappa_s \phi_s$, as a function of the Shields number N_{Sh}

slope. As shown above, the contribution of the saltating particles κ_s depended on the channel slope (at least via the water depth). This prompted us to plot the diagram differently by only reporting the contribution due to the saltating particles, i.e., by plotting $\kappa_s \phi_s$ (see Fig. 16).

Data scattering is here markedly reduced, allowing to fit a curve to the data. The resulting equation is similar to the Meyer-Peter equation, the only difference lies in the values used for the coefficients:

$$\phi_s = 2(N_{Sh} - 0.056)^{3/2}.$$

Contrary to the saltating regime, we failed to find a scaling that would make it possible to collapse the rolling contribution onto a single curve. This result shows that, on steep slopes, bed-load transport due to saltation can be reasonably well described using a power law with a threshold while a different approach is needed for the rolling motion.

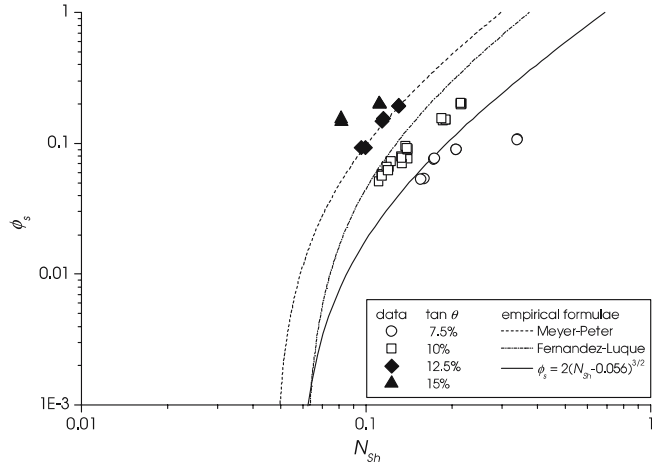

Fig. 15 Dimensionless solid discharge ϕ_s as a function of the Shields number N_{Sh}

An image sequence of the particle transport is available in the audiovideo interleave (AVI) format in Electronic Supplementary Material. This animation is a 130-frame excerpt of the filmed particle transport. The original duration of the slow motion sequence is 1 s. See Table 4 column E10-8 and Fig. 2 for experimental conditions.

7 Conclusion

In this paper, we detailed a method to analyze bed load transport experiments on a mobile bed with image processing techniques. We used an inclined channel in which particle and water supplies at the inlet were controlled accurately. As the channel was only slightly wider than the diameter of the monosized spherical particles, their motion was approximately two-dimensional. These simplifications were necessary as they allowed us to film the individual movement of all particles with a high speed camera (on the order of 100 individuals per image). The images were analyzed combining image-processing operations to detect particle positions. A particle-tracking algorithm was developed to obtain the trajectories and the motion regimes, rolling or saltation. Another image-processing algorithm made it possible to detect the water line.

We were thus able to calculate hydrodynamic and sedimentologic variables. The water line was marked by fast surface waves, while the bed elevation was characterized by sporadic rearrangements in the bed. Secondly we investigated the contribution of the rolling and saltating regime by analyzing the vertical transport profiles. At a constant slope of 10% the contribution of the rolling particles to the solid discharge was substantial but only slightly differed when the particle supply increased. When the slope increased, rolling became the major regime. When the solid flow rate was broken down, respectively, into the rolling and the saltating

contribution, we found that slope has little effect on the transport of saltating particles, which makes it possible to derive a single curve linking the solid discharge and the Shields number in a way similar to empirical formulas such as Meyer-Peter's equation. On the contrary, no scaling could be found for the rolling regime.

Since the saltation of a single particle has provided up to now the theoretical support to empirical bed-load equations (Bagnold 1973; Bridge and Dominic 1984; Wiberg and Smith 1985; Sekine and Kikkawa 1992; Seminara et al. 2002), we can wonder whether the rolling regime has not been neglected at least on steep slopes. We hope that these results giving valuable insights into the mechanisms of bed load transport will help developing better particle-based bed load transport models.

Acknowledgments This study was supported by the Cemagref and funding was provided by *Programme Avenir* of the Rhône Alpes Région, by *Action Concertée Incitative* "Risques naturels" and by the *Programme national risque hydrologique* INSU /ECCO of the CNRS. We are grateful to the TSI laboratory (Nathalie Bochard, Jacques Jay, and Jean-Paul Schon).

References

Ancey C, Bigillon F, Frey P, Ducret R, Lanier J (2002) Saltating motion of a bead in a rapid water stream. Phys Rev E 66:036306

Ancey C, Bigillon F, Frey P, Ducret R (2003) Rolling motion of a bead in a rapid water stream. Phys Rev E 67:011303

Bagnold R (1973) The nature of saltation and of 'bed load' transport in water. Philos Trans R Soc Lond Ser A 332:473–504

Barat C, Ducottet C, Jourlin M (2003) Pattern matching using morphological probing. In: IEEE ICIP 2003, Barcelona, Spain

Böhm T (2005) Motion and interaction of a set of particles in a supercritical flow. PhD Thesis, Université Joseph Fourier, France

Böhm T, Ancey C, Frey P, Reboud J, Ducottet C (2004) Fluctuations of the solid discharge of gravity-driven particle flows in a turbulent stream. Phys Rev E 69:061307

Böhm T, Ancey C, Frey P, Jodeau M, Reboud J (2005) Experiments on gravity-driven particle flows in a turbulent stream. In: Powders and grains, proceedings of the 5th international conference on micromechanics of granular media, Stuttgart, Germany. Balkema publishers, Rotterdam, pp 1001–1004

Bridge J, Dominic D (1984) Bed load grain velocities and sediment transport rates. Water Resour Res 20:476–490

Courtney J (1997) Automatic video indexing via object motion analysis. Pattern Recognit 30:607–625

Drake T, Shreve R, Dietrich W, Whithing P, Leopold L (1988) Bedload transport of fine gravel observed by motion-picture photography. J Fluid Mech 192:193–217

Economikos L, Shoemaker C, Russ K, Jones D (1990) Toward full-field measurements of instantaneous visualizations of coherent structures in turbulent shear flows. Exp Therm Fluid Sci 3:74–86

Fernandez Luque R, van Beek R (1976) Erosion and transport of bed-load sediment. J Hydraul Res 14:127–144

Frey P, Reboud J (2001) Experimental study of narrow free surface turbulent flows at steep slopes. In: Ninokata H, Wada A, Tanaka N (eds) Advances in flow modeling and turbulence measurements. World Scientific, Singapore, pp 217–224

Frey P, Ducottet C, Jay J (2003) Fluctuations of bed load solid discharge and grain size distribution on steep slopes with image analysis. Exp Fluids 35:589–597

Gonzalez R, Woods R (1992) Digital image processing, 2nd edn. Addison Wesley, Reading

Hu C, Hui Y (1996a) Bed-load transport. I: Mechanical characteristics. J Hydraul Eng-ASCE 122:245–254

Hu C, Hui Y (1996b) Bed-load transport. II: Stochastic characteristics. J Hydraul Eng-ASCE 122:255–261

Hwang V (1989) Tracking feature points in time-varying images using an opportunistic selection approach. Pattern Recogn 22:247–256

Lee H, Chen Y, You J, Lin Y (2000) Investigations of continuous bed load saltating process. J Hydraul Eng-ASCE 126:691–700

Meyer-Peter E, Müller R (1948) Formulas for bed-load transport. In: Int. Assoc. Hydraul. Res., 2nd meeting, Stockholm, pp 39–64

Niño Y, García M, Ayala L (1994) Gravel saltation, 1. experiments. Water Resour Res 30:1907

Nishino K, Kosagi N, Hirata M (1989) Three-dimensional particle tracking velocimetry based on automated digital image processing. J Fluids Eng Trans ASME 111(11):384–391

Okamoto K, Hassan Y, Schmidl W (1995) New tracking algorithm for particle image velocimetry. Exp Fluids 19:342–347

Papanicolaou AN, Diplas P, Balakrishnan M, Dancey CL (1999) Computer vision technique for tracking bed load movement. J Comput Civil Eng 13(2):71–79

Pilotti M, Menduni G, Castelli E (1997) Monitoring the inception of sediment transport by image processing techniques. Exp Fluids 23(3):202–208

Salari V, Sethi I (1990) Feature point correspondence in the presence of occlusion. IEEE Trans Pattern Anal Mach Intell 12:87–91

Schmeeckle M, Nelson J (2003) Direct numerical simulation of bedload transport using a local, dynamic boundary condition. Sedimentology 50:279–301

Sekine M, Kikkawa H (1992) Mechanics of saltating grains 2. J Hydraul Eng 118(4):536–558

Seminara G, Solari L, Parker G (2002) Bed load on arbitrarily sloping beds: failure of the Bagnold hypothesis. Water Resour Res 38:1249

Sethi I, Jain R (1987) Finding trajectories of feature points in a monocular image sequence. IEEE Trans Pattern Anal Mach Intell 9(1):56–73

Soille P (1999) Morphological image analysis, principles and applications. Springer, Berlin Heidelberg New York

Udrea D, Bryanston-Cross P, Querzoli G, Moroni M (2000) Fluid mechanics and its application: chapter particle tracking velocimetry techniques. Kluver, The Netherlands, pp 279–304

Wiberg P, Smith J (1985) A theoretical model for saltating grains in water. J Geophys Res 90:7341–7354

Willert C, Gharib M (1991) Digital particle image velocimetry. Exp Fluids 10:181–193